

Efficient 3'-pairing renders microRNA targeting less sensitive to mRNA seed accessibility

David M. Kosek¹, Elnaz Banijamali², Walter Becker², Katja Petzold^{2,3,*} and Emma R. Andersson^{1,*}

¹Department of Cell and Molecular Biology, Karolinska Institute, Biomedicum 9B, Solnavägen 9, 17177 Stockholm, Sweden

²Department of Medical Biochemistry and Biophysics, Karolinska Institute, Biomedicum 9B, Solnavägen 9, 17177 Stockholm, Sweden

³Department of Medical Biochemistry and Microbiology, Uppsala University, Biomedical Centre D9:3, Husargatan 3, 752 37 Uppsala, Sweden

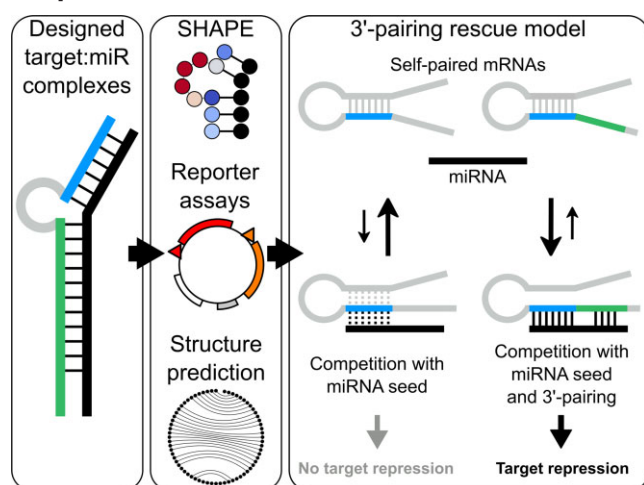
*To whom correspondence should be addressed. Tel: +46 852487360; Email: emma.andersson@ki.se

Correspondence may also be addressed to Katja Petzold. Tel: +46 738304003; Email: katja.petzold@imbim.uu.se

Abstract

MicroRNAs (miRNAs) are short RNAs that post-transcriptionally regulate gene expression by binding to specific sites in mRNAs. Site recognition is primarily mediated by the seed region (nucleotides g2–g8 in the miRNA), but pairing beyond the seed (3'-pairing) is important for some miRNA:target interactions. Here, we use SHAPE, luciferase reporter assays and transcriptomics analyses to study the combined effect of 3'-pairing and secondary structures in mRNAs on repression efficiency. Using the interaction between *miR-34a* and its *SIRT1* binding site as a model, we provide structural and functional evidence that 3'-pairing can compensate for low seed-binding site accessibility, enabling repression of sites that would otherwise be ineffective. We show that miRNA 3'-pairing regions can productively base-pair with nucleotides far upstream of the seed-binding site and that both hairpins and unstructured bulges within the target site are tolerated. We use SHAPE to show that sequences that overcome inaccessible seed-binding sites by strong 3'-pairing adopt the predicted structures and corroborate the model using luciferase assays and high-throughput modelling of 8177 3'-UTR targets for six miRNAs. Finally, we demonstrate that *PHB2*, a target of *miR-141*, is an inaccessible target rescued by efficient 3'-pairing. We propose that these results could refine predictions of effective target sites.

Graphical abstract



Introduction

MicroRNAs (miRNAs) are small non-coding RNAs (~22nt) that function as posttranscriptional regulators of gene expression. MiRNAs bind Argonaute (Ago) proteins to form an RNA-induced silencing complex (RISC), with the miRNA acting as a guide that recognizes mRNAs via base-pairing, leading to decreased expression of the gene product. Gene regulation by miRNAs is prevalent, with more than half of hu-

man mRNAs containing at least one conserved binding site for a miRNA (1), yet it is not fully understood how target site selection and efficiency of downregulation is affected by the structure of the mRNA:miRNA complex or by pre-existing structures on the mRNA side (2–11), resulting in suboptimal prediction of downregulation efficiency.

In most animals, miRNAs do not require full sequence complementarity to repress target mRNAs (12). Instead, target

Received: July 21, 2022. Revised: September 15, 2023. Editorial Decision: September 18, 2023. Accepted: September 19, 2023

© The Author(s) 2023. Published by Oxford University Press on behalf of Nucleic Acids Research.

This is an Open Access article distributed under the terms of the Creative Commons Attribution-NonCommercial License

(<http://creativecommons.org/licenses/by-nc/4.0/>), which permits non-commercial re-use, distribution, and reproduction in any medium, provided the original work is properly cited. For commercial re-use, please contact journals.permissions@oup.com

recognition is initiated by binding to the miRNA ‘seed’ region, comprising nucleotides 2–8 of the guide RNA (referred to as g2–g8) (Figure 1A). The complementary ‘seed-binding site’ in the mRNA is the most conserved element of miRNA targets in animals (13,14) and the basis for widely used site prediction algorithms such as TargetScan (15). MiRNAs with identical seed sequences are grouped into families, whose members share a subset of their target genes through common seed pairing (16,17). Although binding of the seed alone is sometimes sufficient for effective downregulation (18–21), pairing of miRNA nucleotides outside the seed (referred to here as the 3′-pairing region, starting from the g9 residue) can contribute to increased target repression (2,19) and act as a determinant of targeting specificity within miRNA families (4,6,22). Structural data show that binding of a seed-matched target to RISC induces a conformational shift in helix 7 of the Ago protein, which exposes nucleotides g13–g16 (known as the supplementary region) for potential pairing in a comparable way as the seed region in guide-only structures (23,24). It has also been demonstrated that strong 3′-pairing may compensate for mismatches or nucleotide bulges in the seed region, referred to as 3′-compensatory pairing (19,25). These findings suggest that 3′-pairing can be an important factor for miRNA target specificity and efficacy.

In addition to the sequence complementarity between the miRNA and target site, the degree of repression can be affected by the formation of secondary structures in the mRNA making the seed-binding site of the target inaccessible to the miRNA (26–28). The observed statistical tendency for effective sites to reside in AU-rich regions (2) could plausibly be related to decreased formation of stable blocking structures, and it has recently been proposed that RNA-binding proteins broadly function to open up mRNA structures, enabling regulation by miRNAs (29). However, less is known about the potential interplay between 3′-pairing and secondary structures in the mRNA, present prior to miRNA binding or formed as part of the target:miRNA complex, in determining the final outcome of miRNA-mediated repression.

A structural model of the guide RNA of the conserved *miR-34a* (30) bound to a validated target site in the transcript of *silent information regulator 1* (*SIRT1*) (31) has recently been solved by NMR and its dynamics described (8). In this structure, a ground state of a seven-nucleotide seed helix was found to exist in equilibrium with a transient excited state (ES) in which the seed helix is extended by a closing G:U base-pair at the 3′-end (Figure 1B, C). Simulations showed that the altered seed shifts the bending angle between the seed and 3′-pairing helices, suggesting a model in which RISC undergoes a transition after binding to the seed, allowing the *miR-34a* 3′-pairing region to pair with complementary residues in the *SIRT1* mRNA (see also (32)). Mutating the site to create a canonical eight-nucleotide seed helix resulted in base-pairing and interhelical bending angles identical to the excited state.

Here, we study the effect of 3′-pairing on repression of mRNA target sites with a range of different structures, using the interaction between *miR-34a* and *SIRT1* as a model system. We use luciferase reporter assays to quantify downregulation, RNA:RNA binding by SHAPE (RABS) (33) to determine base-pair formation in target sites in the presence or absence of miRNA binding, and analysis of deposited transcriptomics data to validate hypotheses. Based on measured repression of sites with different degrees of 3′-pairing and computational predictions of binding energy, we propose a model

in which pairing beyond the seed has the capacity to compensate for a structurally inaccessible seed. We experimentally test this model using an artificial and a natural target:miRNA interaction, and provide structural and functional data demonstrating that 3′-pairing can overcome the energetic penalty imposed by low seed-binding site accessibility, enabling repression of sites which are non-functional when seed pairing alone is available.

Materials and methods

Cell culture

HEK293T cells (ATCC) were cultured in Dulbecco’s modified essential medium (DMEM, Gibco) supplemented with 10% fetal bovine serum (FBS, Gibco). The cells were tested for mycoplasma contamination (MycoplasmaCheck, Eurofins), and were mycoplasma-free.

Cloning of reporter plasmids

For dual luciferase reporter assays, we generated plasmids containing the *SIRT1* target site and a number of mutant sites ranging from 22 to 67 nucleotides in length (Supplementary Table S1). Target sites were cloned into a psiCHECK2 vector between the XhoI and NotI restriction sites. The plasmid was cleaved by XhoI (NEB, #R0146) and NotI (NEB, #R3189) in CutSmart buffer (NEB, #B7204) with calf intestinal phosphatase (NEB, #M0290). Cleavage products were separated on a 1% agarose gel and the linearized plasmid was purified with QIAquick Gel Extraction Kit (Qiagen, #28706). Complementary synthetic DNA oligos coding for the target sites, with restriction site overhangs for XhoI and NotI, were purchased from IDT. Inserts were phosphorylated by incubation with T4 polynucleotide kinase (NEB, #M0201) in T4 DNA ligase buffer (NEB, #B0202) at 37°C for 30 min, and then annealed by heating to 95°C for 5 min followed by incubation at room temperature. Annealed inserts were ligated into the vector with T4 DNA ligase (NEB, #M0202) in T4 DNA ligase buffer, with 20 min incubation at room temperature. Ligated vectors were transformed into competent bacteria (One Shot TOP10 *Escherichia coli*; Invitrogen) and grown overnight on ampicillin plates. Selected colonies were grown overnight in LB medium and plasmids were purified using PureLink Plasmid Miniprep Kit (Invitrogen, #K210011) or Qiagen Plasmid Midi Kit (Qiagen, #12145). Correct insertions were verified by Sanger sequencing (LightRun, Eurofins). The psiCHECK2 vector was a gift from J. Weidhaas (Addgene plasmid #78258; <http://n2t.net/addgene:78258>; RRID:Addgene_78258) (34).

miRNA oligo preparation for reporter assays

Synthetic guide and passenger strands for *hsa-miR-34a-5p* and *hsa-miR-141-3p* were purchased from IDT, resuspended in nuclease-free duplex buffer (30 mM HEPES, pH 7.5; 100 mM potassium acetate) (IDT, #11-01-03-01) and annealed by heating to 95°C for 2 min followed by incubation at room temperature. The nucleotide sequences for each strand are listed in Supplementary Table S2. Guide strands were ordered with 5′-phosphorylation.

Dual luciferase reporter assays

HEK293T cells were seeded in 24-well plates 24 h prior to transfection. At 80–90% confluency, cells were either trans-

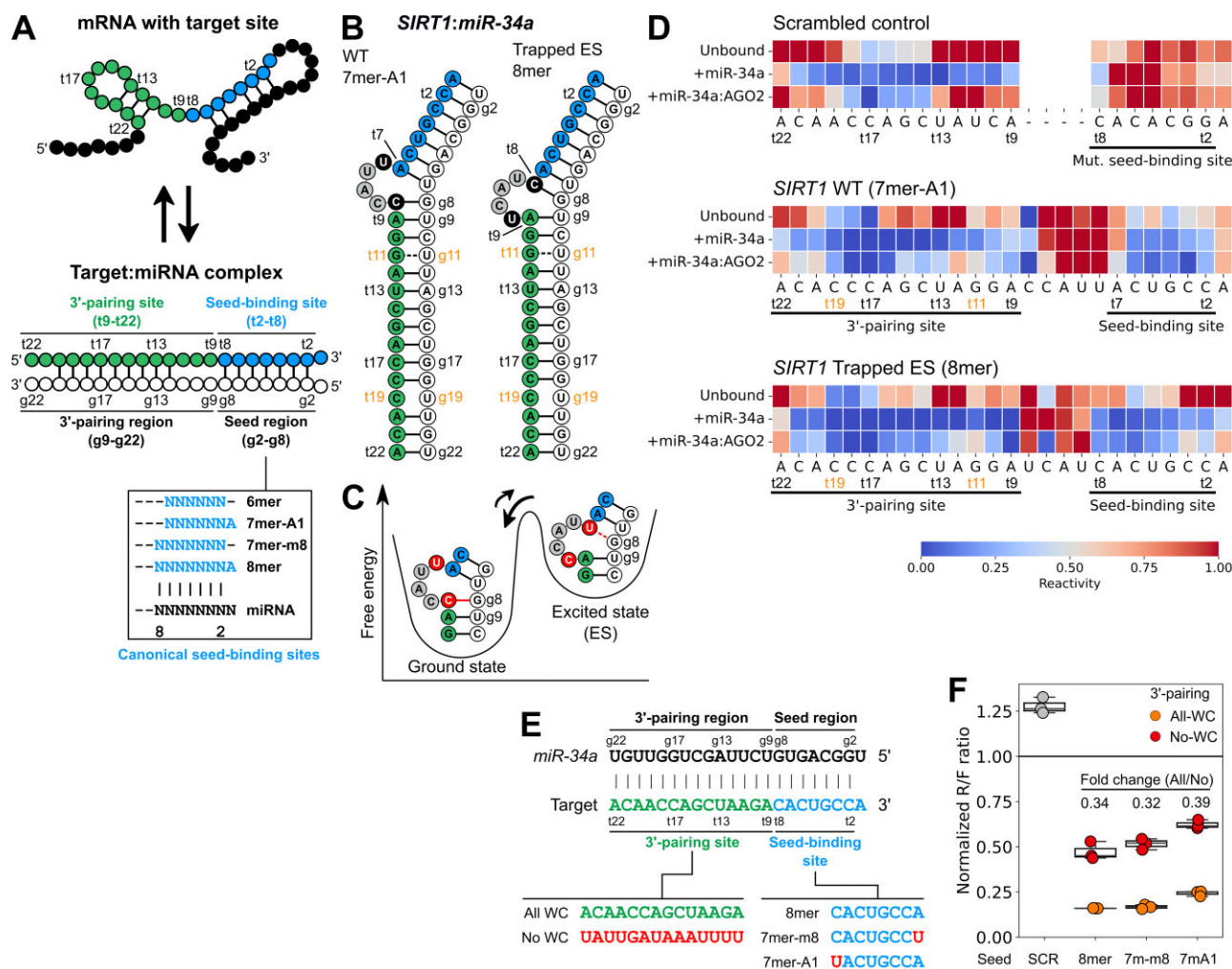


Figure 1. The *SIRT1:miR-34a* complex as an experimental model. **(A)** Schematic of a target:miRNA interaction, with target site unfolding followed by miRNA binding. The seed-binding and 3'-pairing sites are shown in blue and green respectively. Canonical seed-binding sites are shown in the box (N represents an arbitrary nucleotide). **(B)** Secondary structure of the wild-type *SIRT1:miR-34a* complex (left) and the trapped excited state (right). Mutated residues in black. **(C)** Seed dynamics of the *SIRT1:miR-34a* complex. **(D)** Mean RABS reactivities ($n = 3$) of nucleotides in a scrambled target site (top) wild-type *SIRT1* (middle) and the trapped excited state ('ES'; bottom), in unbound form or bound to *miR-34a* or *miR-34a:AGO2*, where reactivities below 0.5 indicate base-pairing. **(E)** Sequences of *miR-34a* target sites with 8mer, 7mer-m8 and 7mer-A1 seed regions, with or without fully complementary 3'-pairing. **(F)** *miR-34a* regulation of dual luciferase reporters after 24 h with the target sites in **(E)**, transfected into HEK293T cells. Each datapoint represents an independent experiment ($n = 3$). SCR is a seed-scrambled control. Fold changes are calculated from mean normalized Renilla/Firefly ratios.

fectured with 0.8 μ g plasmid and 0 or 30 nM *hsa-miR-34a* duplex, using Lipofectamine 2000 (Invitrogen) in Opti-MEM (Gibco) according to the manufacturer's protocol. After 24 h incubation, cells were washed once with 0.1 ml phosphate-buffered saline (PBS) and luciferase activity was measured with the Dual Luciferase Reporter Assay System (Promega, E1910) according to the manufacturer's instructions. Measurements were made on a Promega GloMax 96 luminometer with 1 s delay and 10 s integration time. For each sample, the signal from *Renilla* luciferase (carrying the miR target site) was normalized to the signal from *Firefly* luciferase. For each plasmid, the Renilla/Firefly (R/F) ratio of the 30 nM *miR-34a* sample was normalized to the R/F ratio of the 0 nM *miR-34a* sample. In each experiment, a negative control plasmid with a scrambled seed region (referred to as SCR) was included (sequence in Supplementary Table S1). Statistical analysis was performed with *scipy* (version 1.10.1; one-way ANOVA, using the function *stats.f_oneway*) and *statsmodels* (version 0.13.5; Tukey's Honestly Significant Difference, func-

tion *stats.multicomp.pairwise_tukeyhsd*). Hierarchical clustered heatmaps were generated with *seaborn* (version 0.12.2; function *clustermap*). All reporter assay measurements can be found in Supplementary File 1.

Preparation of *miR-34a:AGO2* for RABS assays

The *AGO2* gene was cloned into a pFastBac expression vector (Thermo Fisher), with an amino-terminal His-tag followed by a TEV cleavage site. The vector was transformed into DH10EmBacY cells (Geneva Biotech) to generate a recombinant bacmid, which was confirmed by blue/white screening, bacmid isolation and PCR analysis. Sf9 cells were transfected with recombinant bacmid (P0-AGO2), with amplification through two rounds of additional transfections (P1-AGO2 and P2-AGO2). 300 mL P2-AGO2 baculovirus stock was filtered and FBS was added to a final concentration of 2%. *AGO2* overexpression was verified by Western blot (Abcam, anti-6X His-tag AB [ab18184]).

Sf9 cells grown in Sf-900 II SFM media (Thermo Fisher) were transduced with P2-AGO2 baculovirus stock, followed by expression of AGO2 for ~72 h at 27°C in an orbital shaker. Pelleted cells were washed with PBS and resuspended in IMAC buffer A (50 mM Tris-HCl, 300 mM NaCl, 10 mM Imidazole, 1 mM TCEP, 5% glycerol v/v), to which 25× EDTA-free protease inhibitor cocktail (Merck) was added. Cells were lysed by three freeze-thaw cycles on dry ice, sonicated for 10 min (30% amplitude, 10 sec ON, 10 sec OFF) and centrifuged for 1 h at 50 000 RCF and 4°C. The supernatant was passed through a 0.22 µm sterile filter and applied to a HisTrap-Ni 2+ columns (Cytiva, HisTrap HP) preequilibrated with IMAC buffer A. A linear gradient was applied with buffer A and buffer B (50 mM Tris-HCl, 300 mM NaCl, 300 mM Imidazole, 1 mM TCEP, 5% glycerol). Protein-containing fractions were pooled and concentrated with a 30 kDa cut-off Amicon centrifugal filter unit (Sigma Aldrich). Next, AGO2 was incubated with *in vitro* transcribed *miR-34a* at 37°C for 4–5 h to allow loading of guide RNA. The loaded protein solution was dialyzed (Spectrum, 3000 MWCO). After addition of 200 µl TEV, the solution was dialyzed against 2 l IMAC buffer A overnight at 8°C. Following centrifugation, the supernatant was loaded onto a HisTrap-Ni 2+ column to remove TEV-protease and other impurities. The flowthrough was applied to a size exclusion chromatography (SEC) column (Cytiva, HiLoad 16/600 Superdex 200 pg) preequilibrated with buffer C (20 mM HEPES, 100 mM KCl, 1 mM TCEP, 5% glycerol). All fractions of HisTrap-Ni 2+ columns and SEC were analyzed by SDS-PAGE (Thermo Fisher, NuPAGE 4 to 12%, Bis-Tris, 1.0 mm). The protein concentration was determined by a Bradford-based assay (Thermo Fisher, Pierce Detergent Compatible Bradford Assay Kit) using BSA as standard. Loading of guide RNA into AGO2 was assessed by Northern blot (35).

RNA-RNA binding by SHAPE (RABS)

The design and preparation of RNA scaffolds was carried out as previously described (33). mRNA sequences were inserted into the target region of the main loop (Supplementary Figure S1A) and DNA templates were produced with primer assembly and the Primerize web server (36). Phusion High-Fidelity PCR Master Mix with HF buffer (Thermo Fisher) was used to amplify each DNA template. Then, the RNA scaffolds were *in vitro* transcribed (each reaction (V_t = 100 µl): 100 mM Tris-HCl pH 8.0, 10 mM MgCl₂, 10 mM dithiothreitol, 20 mM spermidine, 5 mM GMP, 3 mM NTPs, 0.3 mg/ml T7 polymerase (inhouse produced) (37), 0.1 mg/ml inorganic pyrophosphatase (iPPase, inhouse produced) (38), 3.6 ng/ml of dsDNA template), and purified using RNAClean XP beads (Beckman Coulter).

RABS probing of the unbound construct, followed by probing of binding of the second component (*miR-34a* or AGO2 loaded with *miR-34a*) was monitored by capillary electrophoresis (Supplementary Figure S1B). For RABS probing and primer extension we followed the protocol of Cordero *et al.* (39). The RNA scaffolds were folded in Na-HEPES buffer (pH 8), for 3 min at 95°C, 30 min on ice, followed by 30 min incubation at room temperature (final concentration per reaction (V_t = 15 µl): 0.08 µM RNA, 67 mM Na-HEPES, 10 mM MgCl₂). For each scaffold, 8 reactions were included: (i) a control reaction with no RNA modifier; (ii) 3 reactions (technical replicates) with RNA modifier (1-methyl-7-nitroisatoic anhydride (1M7) (40)); (iii) 4 reactions with no

RNA modifier, used as Sanger ladders. 1.72 µl of 1M7 (from 100 µM stock) were added per reaction to those containing RNA modifier. For reactions containing no modifier, the same volume of ddH₂O was added to adjust the total volume. To recover the RNA scaffold, 9.8 µl of Recovery mix (0.25 M Na-MES (pH 6), 1.5 M NaCl, 0.006 µM 5'-poly-dA-FAM-labeled primers (IDT), 1.5 µl poly-dT Dynabeads (Thermo Fisher)) was added per reaction. After 3 washing steps with 70% ethanol (each time 100 µl) and air drying, 2.5 µl of ddH₂O and 2.5 µl of reverse transcription (RT) mix (1 µl 5× First strand buffer (Thermo Fisher), 0.01 M DTT, 1.6 mM dNTPs, 0.1 µl SuperScript III Reverse Transcriptase (Thermo Fisher)) were added to all reactions but the sequencing ladder. For the Sanger sequencing ladder reactions, separate RT mixes were prepared, using a 1:6 ratio of dNTPs:ddNTP. For the RT step, all samples were incubated at 50°C for 30 min. Next, for RNA hydrolysis, 5 µl of NaOH (0.4 M) was added, then samples were incubated at 90°C for 3 min, and cooled on ice for another 3 min. To neutralize the pH, 5 µl of Acid mix (1 volume of 1.25 M NaCl, 1 volume of 0.5 M HCl, 2 volumes of 1 M NaOAc) was added per reaction. To purify the cDNA, samples were washed 3 times with 70% ethanol (each time 100 µl) followed by 1 h of airdrying at room temperature. The cDNA was eluted from Dynabeads by adding 11 µl of Formamide-ROX mix (1000 µl Hi-Di Formamide (Thermo Fisher), 8 µl of 350 ROX size standard (Thermo Fisher)) per reaction and incubating at room temperature for 15 min. Finally, the samples for capillary electrophoresis were prepared in two different dilutions—‘saturated samples’ (1:2 dilution of the eluted cDNA with Formamide-ROX mix) and ‘diluted samples’ (1:15 dilution of the eluted cDNA with Formamide-ROX mix).

RABS experiments were performed for *miR-34a* or human Argonaut protein 2 (AGO2) loaded with *miR-34a* (AGO2:*miR-34a*). The second component (i.e. *miR-34a* or AGO2:*miR-34a*) was added after re-folding of the mRNA target scaffold (after the first ice incubation step). For experiments with *miR-34a* only, a 1:2 RNA scaffold:*miR-34a* ratio was used. For experiments with AGO2:*miR-34a*, a 1:1 RNA scaffold:AGO2:*miR-34a* ratio was used. After 1M7-modification, described above, 45 µl of proteinase K (PK) mix (20 µg proteinase K PCR grade (Sigma Aldrich), 50 mM Tris-HCl pH 7.5, 75 mM NaCl, 6.25 mM EDTA, 1% SDS (w/v)) was added per reaction and the samples were incubated at 65°C for 1 h to digest the AGO2 protein. After inactivating proteinase K (120 µl of 70% ethanol, followed by 5 min incubation on ice), 19.6 µl of Recovery mix was added. per reaction.

Capillary electrophoresis profiles were analyzed using the HiTRACE pipeline (41). Reactivity values of the nucleotides in the main loop were normalized to the averaged reactivity values of the buffer nucleotides, the nucleotides before and after the target sequence in the main loop (Supplementary Figure S1A). The reactivity was limited to 0–1 (42), which addresses the question of base-pairing while eliminating negative reactivity due to averaging artifacts and large positive values, representing different levels of dynamics, which are not relevant in this context. In line with previous work (43), we use a reactivity value of 0.5 as a cutoff for probable base-pairing, with nucleotides above this value considered likely to be unpaired. This was previously verified for the wild-type *SIRT1:miR-34a* complex by NMR (8). Raw and processed RABS data can be found in Supplementary File 2.

Secondary structure predictions of luciferase constructs

Modules from the ViennaRNA package (44) were used for prediction of the secondary structures of miRNA-target complexes. The energy of binding between *miR-34a* and a target site was predicted with the RNAfold module. The impact of mRNA unfolding on interactions with *miR-34a* was predicted with the RNAup module, using the full-length mRNA sequence of Renilla luciferase from the psiCHECK2 plasmid, including the 3'-UTR containing the miRNA binding site. For both RNAfold and RNAup predictions, pairing to specific regions of the miRNA was disallowed by means of a constraint on the prediction (using the `-constraint` argument). For all RNAup runs, pairing to the seed (residues g1–g7) was enforced to avoid off-target predictions. Correlation coefficients between predicted binding energies and luciferase reporter data were computed with the `scipy` Python library (version 1.10.1; using the function `scipy.stats.linregress`). Illustrations of secondary structures were drawn with StructureEditor from the RNAstructure package (45). Predicted structures and energies are provided in Supplementary File 3. Analysis code is provided in Supplementary File 4.

Analysis of deposited transcriptomics data

The analysis was performed on a microarray dataset measuring the transcriptomic response to transfections of seven miRNAs in HCT116 cells at 24 h (46). Log₂ fold changes were downloaded from Agarwal *et al.* (Supplementary File 2 from (15)). One miRNA (*miR-200b*) was excluded from the analysis as the TargetScan database does not list it as a confidently annotated miRNA. Target site predictions, miRNA sequences and UTR sequences were downloaded from TargetScan (https://www.targetscan.org/cgi-bin/targetscan/data_download.vert80.cgi). Modules from the ViennaRNA package were used for structure predictions. For each miRNA, genes with a single 8mer or 7mer seed-binding site were analyzed. For prediction of 3'-pairing, we searched for perfect matches to at least four continuous residues in the g12–g17 region of the miRNA, with a maximum offset of four nucleotides. For each site, the unfolding energy of eight nucleotides spanning the seed-binding site ($\Delta G_{\text{unfolding}}$) was predicted with RNAup. To save computational time, the predictions were limited to a sequence window with 150 nucleotides flanking the seed in both directions (upstream and downstream). This likely covers most secondary mRNA structures affecting the miRNA binding site (see (47) on optimizing accessibility predictions for siRNA design). The seed-binding energy ($\Delta G_{\text{binding}}$) was predicted for each seed type of the miRNAs with RNAeval. Target genes were binned according to the overall strength of the predicted seed interaction ($\Delta G_{\text{unfolding}} + \Delta G_{\text{binding}}$). Statistical analyses were performed with `scipy` (version 1.10.1; one-way ANOVA, function `stats.f_oneway` and Wilcoxon's test, function `stats.ranksums`). Analysis code is provided in Supplementary File 4.

Prediction of inaccessible seed-binding sites for experimental validation

Target site predictions, miRNA sequences and UTR sequences were downloaded from the TargetScan database (https://www.targetscan.org/cgi-bin/targetscan/data_download.vert80.cgi). Modules from the ViennaRNA package were used for structure predictions. For 8mer and

7mer sites for miRNAs labelled as broadly conserved in the database, we predicted pairing between the miRNA 3'-end (residue g9 and beyond) and 24 nucleotides immediately upstream of the seed with the RNAsubopt module and retained minimum free energy (MFE) structures meeting a set of criteria (full pairing to g13–g16, no mismatches, no GU wobble pairs, at most four bulged nucleotides on the target side). For sites with 3'-pairing, we predicted locally stable structures in the 3'-UTR with the RNALfold module, allowing a maximum base-pair span of 100 nucleotides. Unique target site folds were extracted from the ensemble of structures. For these, we calculated the number of bases in the seed paired downstream, the MFE of the fold (using the RNAeval module) and the frequency of the fold in the full ensemble of structures spanning the target site predicted by RNALfold. Analysis code is provided in Supplementary File 4.

Results

Secondary structure of the *SIRT1:miR-34a* complex

Interactions between miRNAs and their target sites are initiated by binding to the seed region (48,49), comprising nucleotides 2–8 of the guide RNA (referred to as g2–g8, numbered from the 5' end). The formation of the target:miRNA complex may require unfolding of existing mRNA secondary structure to expose the seed-binding site for interaction with the miRNA (Figure 1A, top structure). Sometimes seed-binding is followed by pairing to the remainder of the miRNA, referred to as the 3'-pairing region (starting at residue g9), if complementary target residues are available upstream of the seed-binding site (Figure 1A, lower structure). When present, residues predicted to bind the miRNA 3'-pairing region will be referred to as the 3'-pairing site. For the sake of consistency between target sites of different length, we will number target nucleotides from the 3' end, starting with t1, by the guide nucleotide they are predicted to align with in the target:miRNA complex. Most regulation by miRNAs is thought to be mediated by the so-called canonical seed-binding sites, which feature full g2–g7 complementarity (2,12). They are commonly divided into 6mer (g2–g7 match), 7mer-A1 (g2–g7 match with an adenosine opposite g1), 7mer-m8 (g2–g8 match) and 8mer (g2–g8 match with an adenosine opposite g1) sites, in increasing order of average efficiency (Figure 1A).

As a model system to investigate the impact of different structural elements on miRNA-mediated regulation, we chose the *SIRT1:miR-34a* target:miRNA complex, which consists of a 7mer-A1 seed and a strong 3'-pairing helix separated by a four-nucleotide bulge in the target (Figure 1B, left structure). An NMR structural model ((8); described in the Introduction) showed the existence of a transient excited state ('ES', Figure 1C) which can be stabilized by mutation to create a canonical 8mer seed (Figure 1B, right structure). In the model, the seed and 3'-pairing helices of the *SIRT1:miR-34a* complex are separated by a four-nucleotide bulge, whose position shifts by one nucleotide depending on the dynamics of the seed.

We probed the secondary structure of the *SIRT1:miR-34a* complex with RABS (33). The degree of 1M7 reactivity of the nucleotides inversely reflects binding to the target RNA and was determined for a scaffold carrying the *SIRT1* sequence alone, and in the presence of guide RNA (*miR-34a*) or RISC (AGO2 loaded with *miR-34a*) (Supplementary Figure S1A, B).

In a scrambled seed site, containing a mutated seed-binding site but retaining potential pairing to the *miR-34a* 3'-pairing region, there was no reactivity change in the seed-binding site in the presence of *miR-34a* guide RNA or *miR-34a*:AGO2 (Figure 1D, 'Scrambled control', see also (33)). The guide RNA was base-paired outside the seed-binding site, whereas the *miR-34a*:AGO2 complex showed little overall difference compared to the unbound target.

In the wild-type *SIRT1* sequence, the reactivity pattern matched the NMR model, with an overall decrease in reactivity across the seed and 3'-pairing sites, but no reduction in the bulge, in the presence of *miR-34a* or *miR-34a*:AGO2 compared to the unbound state (Figure 1D, 'WT'). The same pattern was observed for the 8mer seed mutant corresponding to the excited state (Figure 1D, 'Trapped ES'; cf. (8)). In the 7mer-A1 seed, the Ug7:At7 closing base pair appears less stable than the other seed pairs, which is also in line with prior NMR data. Consistently low reactivities for repeated cytidine residues, even in the unbound condition, complicated analyses involving these sequences, which is a previously described artefact of this assay (33). Overall, the well-characterized structural properties of this target:miRNA complex makes it a suitable system for exploring the impact of 3'-pairing on target repression.

To determine the baseline repression efficiency of differential seed types alone for *miR-34a* targeting, we cloned sequences with 8mer, 7mer-m8 and 7mer-A1 seeds and either complete or no Watson-Crick (WC) base-pairing to the *miR-34a* 3'-pairing region (g9-g22) (Figure 1E, referred to as all-WC and no-WC respectively) into dual luciferase reporter plasmids. The plasmids were co-transfected with *miR-34a* duplex in HEK293T cells to determine the repression of each target site after 24 h, in three independent experiments. The 8mer and 7mer-m8 seeds were similarly downregulated (0.47 ± 0.05 and 0.52 ± 0.03), to a greater degree than the 7mer-A1 target (0.62 ± 0.024) (Figure 1F, statistical analysis in Supplementary Figure S2A). For each seed type, complete miRNA 3'-pairing increased repression by around three-fold compared to the corresponding seed without 3'-pairing, maintaining differences between the seed types. Nonetheless, all types of 7mer and 8mer seed pairing were sufficient for substantial downregulation relative to the luciferase baseline even in the absence of 3'-pairing (Figure 1F).

The supplementary and tail regions substantially impact repression efficiency

To understand how structural features of target:miRNA complexes interact to determine site efficiency, we first sought to carry out a comprehensive investigation into the impact of different parts of the *miR-34a* 3'-pairing region, in the context of different types of seed-binding sites (7mer-A1 or 8mer) and in the presence or absence of a four nucleotide bulge bridging the seed and 3'-pairing helices. We divided the 3'-pairing site into the central (t9-t12), supplementary (t13-t16) and tail (t17-t22) domains (3) and generated luciferase reporter plasmids carrying target sites in which each of the three domains were mutated to disrupt pairing to the corresponding residues in *miR-34a* (Figure 2A). These mutations will be referred to as ΔC (central), ΔS (supplementary) and ΔT (tail) respectively. The 3'-pairing helix of the *SIRT1*:*miR-34a* complex contains two mismatches: a GU wobble at position 11 and a CU mismatch at position 19. We included sites with the mismatched

nucleotides (referred to as WT) or full complementarity (all-WC). Figure 2B shows the predicted effect of the ΔC , ΔS and ΔT mutations on the binding of *SIRT1* to the *miR-34a* guide RNA.

In the luciferase reporter assay, wild-type *SIRT1*, with a 7mer-A1 seed-binding site and a four-nucleotide bulge, was moderately affected by disruptions in any of the three domains of 3'-pairing (Figure 2C, upper left panel; statistical analysis in Supplementary Figure S2B). The ΔC , ΔS and ΔT mutants all repressed at roughly the same level as the 7mer-A1 seed-only site (Figure 2C, upper left panel, compare blue data points to dotted line indicating seed-only repression). The ΔS and ΔT mutants of the 7mer-A1 all-WC site also achieved downregulation comparable to the seed-binding site alone, though substantially less than the all-WC site with intact S/C/T domains and the ΔC mutant (Figure 2C, upper left panel, orange data points). For bulged sites with the stronger 8mer seed-binding site, there was markedly little difference between the all-WC and WT variants (Figure 2C, upper right panel). Notably, in the presence of a bulge the all-WC ΔS variants were less downregulated than the corresponding WT sites, which was the only observed case of theoretically more favourable pairing resulting in a small decrease in efficiency.

Removing the bulge reduced the difference between the WT and all-WC 3'-pairing variants for 7mer-A1 sites (Figure 2C, lower left panel). The efficiency of the WT site increased without the bulge, and like the all-WC variants it became less sensitive to the ΔC mutation, while ΔS and ΔT regions remained consequential. Targets with an 8mer seed-binding site showed a broadly similar pattern of downregulation with and without the bulge (Figure 2C, upper and lower right panels), regardless of base-pairing differences between the WT and all-WC variants. Interestingly, in the absence of a bulge between the seed and 3'-pairing helices the ΔS mutants were less downregulated than their respective seed-only targets (Figure 2C, lower panels, compare to dotted lines), demonstrating that the differences observed in the reporter assay cannot be fully explained by base-pairing potential alone.

Overall, pairing to the central region (g9-g12) was dispensable for most variants, whereas the supplementary region (g13-g16) was universally consequential. The tail region (g17-g22) generally had a strong impact, with the ΔT mutation sometimes obviating the positive effect of 3'-pairing on downregulation. The relative importance of the three 3'-pairing regions was largely the same regardless of the seed type and the presence of a bulge, the most notable exception being that the ΔS and ΔT mutants were sometimes indistinguishable (Figure 2D). Beyond the 3'-pairing region disruptions, the differences between the sites appear to be driven primarily by seed type, and at least for 8mer seeds secondarily by the presence or absence of a bulge between the seed and 3'-pairing regions (Figure 2D).

Full 3'-pairing distant from the seed increases repression

After investigating the roles of 3'-pairing regions in site efficiency, we next sought to determine the impact of structures contained within the target:miRNA binding complex. The *SIRT1*:*miR-34a* complex contains a four-nucleotide bulge between t7 and t8 (or t8 and t9 in the excited state), separating the seed and 3'-pairing helices. We decided to investigate the impact of this bulge on the outcome of the *SIRT1*:*miR-34a* in-

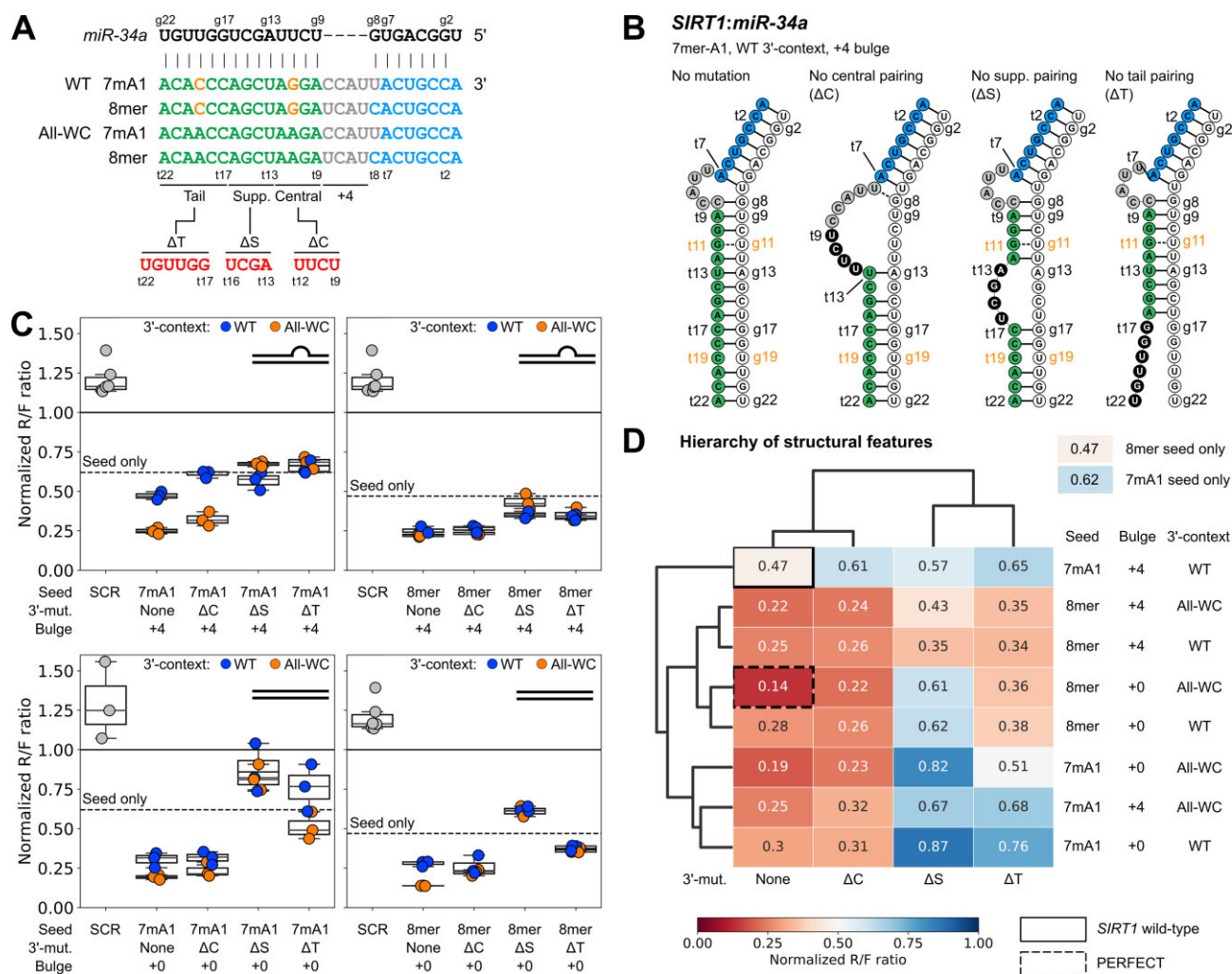


Figure 2. The supplementary and tail regions substantially impact repression efficiency. **(A)** Sequences of *SIRT1* and perfectly complementary target sites with disrupted pairing to the central (ΔC), supplementary (ΔS) or tail (ΔT) regions. **(B)** Predicted secondary structures of *miR-34a* (white) in complex with *SIRT1* target sites with wild-type, ΔC, ΔS and ΔT 3'-end binding sites, with disruptions in black. **(C)** *miR-34a* regulation of dual luciferase reporters after 24 h with the target sites in **(A)**, with indicated mutations, transfected into HEK293T cells. Each datapoint represents an independent experiment ($n = 3$). Lines indicating seed-only pairing, for the corresponding seed type, are based on Figure 1F. SCR is a seed-scrambled control. **(D)** Clustered heatmap of the mean normalized Renilla/Firefly ratio of each site in **(C)**.

teraction, by progressively lengthening the bulge through the addition of uracil nucleotides (Figure 3A, B).

We first wanted to determine how the structure of the *SIRT1:miR-34a* complex is affected by the length of the bulge. To this end, we performed RABS on scaffolds containing sites with bulges from zero to fourteen nucleotides (Figure 3C). For all the *SIRT1* mutants, the presence of RISC or guide RNA resulted in base-pairing in both the seed and 3'-pairing sites relative to the respective unbound target sites. By contrast, the base-pairing propensity in the predicted bulges remained the same or even decreased, suggesting that the nucleotides in the bulges are unstructured. This indicates that even the fourteen-nucleotide bulge can be accommodated by RISC without altering the overall structure of the target:miRNA complex. In the longer bulges (+12 and +14, but also +0) we observe pairing in the bulge and/or 3'-pairing site in the absence of a ligand, suggesting binding within the site or to adjacent regions in the scaffold.

Having shown the capacity for binding of the *miR-34a* 3'-pairing region to residues distant from the seed-binding site,

we next investigated the effect of the different bulge lengths on downregulation efficiency. We therefore cloned the *SIRT1* bulge mutants (with the mismatched WT 3'-pairing site) into a luciferase reporter plasmid, as well as a corresponding set of targets with fully complementary (all-WC) 3'-pairing sites (Figure 3A). There was a clear difference in repression mediated by the WT versus all-WC 3'-pairing regions for target sites containing bulges ranging from zero to fourteen nucleotides (Figure 3D). With bulge lengths between zero and ten nucleotides, full 3'-complementarity resulted in a roughly two-fold increase in downregulation relative to the mismatched 3'-pairing site (Figure 3D).

For targets with mismatched WT 3'-pairing sites, increasing the bulge length from four to six nucleotides was sufficient to decrease downregulation to a similar level as the 7mer-A1 seed-binding site by itself (Figure 3D, compare to dotted lines indicating seed-only repression). Target repression remained at comparable levels with the addition of further uracil residues, with no clear trend towards higher or lower efficiency. The WT 8nt bulge mutant was notably inconsistent

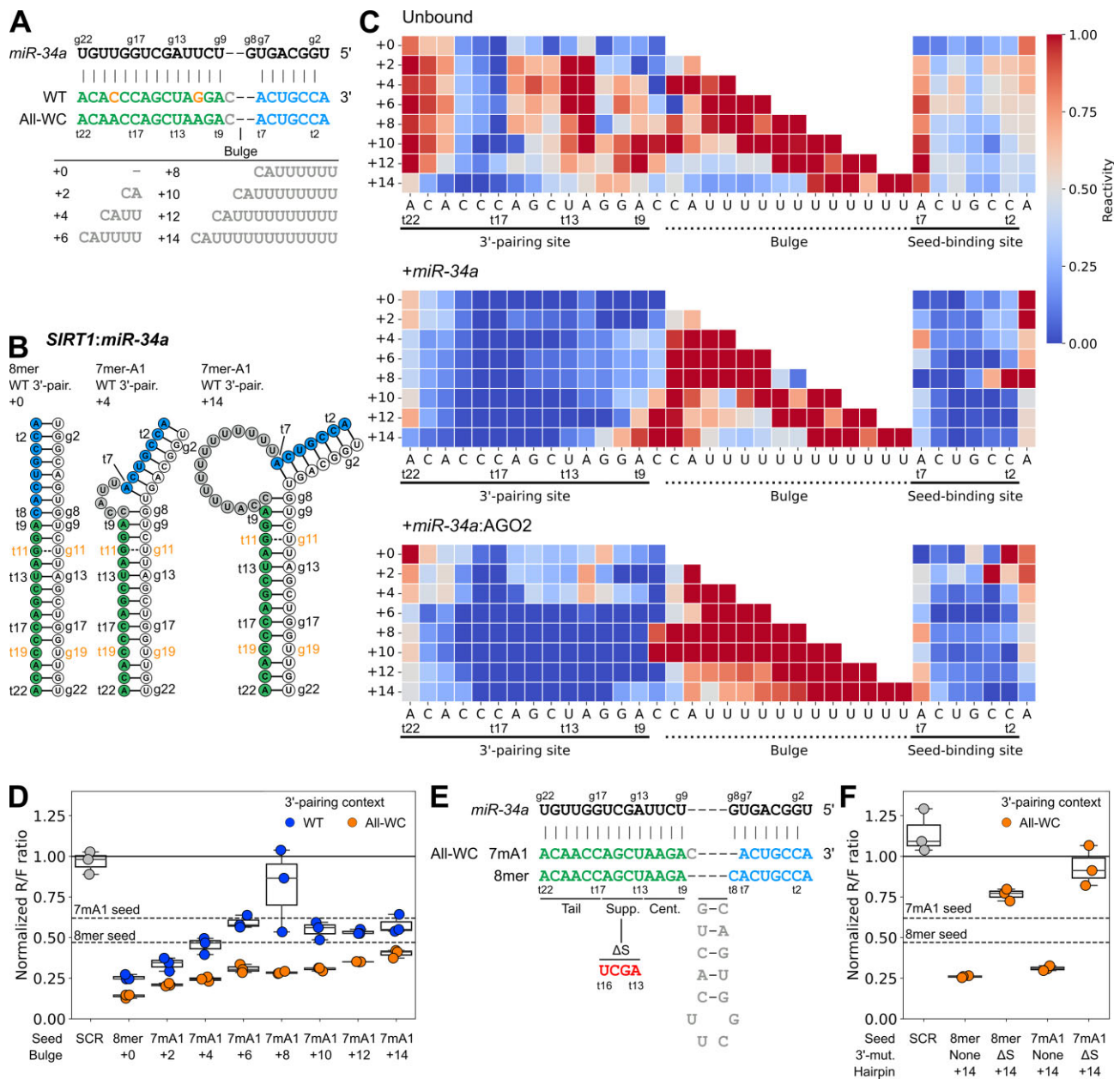


Figure 3. *MiR-34a* 3'-pairing distant from the seed increases site efficiency. **(A)** Sequences of *SIRT1* and perfectly complementary target sites with varying bulge lengths from 0 to 14 nucleotides. **(B)** Predicted secondary structures of *miR-34a* (white) in complex with *SIRT1* target sites with 0, 4 and 14 nucleotide bulges. **(C)** Mean RABS reactivities (n = 3) of nucleotides in *SIRT1* with 0–14 nucleotide bulges, in unbound form (top) or bound to *miR-34a* (middle) or *miR-34a:AGO2* (bottom), where reactivities below 0.5 indicate base-pairing. **(D)** *MiR-34a* regulation of dual luciferase reporters after 24 h with the target sites in (A), with indicated mutations, transfected into HEK293T cells. **(E)** Sequences of target sites with a 14-nucleotide hairpin separating the seed and 3'-pairing regions, with either full or abrogated supplementary (ΔS) 3'-pairing. **(F)** *MiR-34a* regulation of dual luciferase reporters after 24 h with the target sites in (E), with indicated mutations, transfected into HEK293T cells. In (D) and (F), each datapoint represents an independent experiment (n = 3). Lines indicating seed-only pairing are based on Figure 1F. SCR is a seed-scrambled control.

between replicates, but since its RABS reactivity profile was similar to the other targets (Figure 3C) we attribute this to experimental variability rather than a functional difference.

In contrast to the WT sites, all-WC 3'-pairing increased downregulation compared to a seed-only target even with fourteen unpaired nucleotides between t7 and t8. For both WT and all-WC 3'-pairing sites, shortening or fully removing the bulge improved efficiency. In summary, our data provides structural confirmation that RISC can bind targets containing long unstructured bulges and shows that even at a large distance from the seed-binding site individual mismatches in

the central (g9–g12) and tail (g17 and beyond) regions of a miRNA can affect the outcome of an interaction with a target site.

Sites containing hairpin structures can be efficiently repressed

Because long-distance target sites containing unstructured bulges can be downregulated by miRNA, though with decreasing efficiency as the bulge gets longer (Figure 3D), we next asked if miRNAs are also capable of downregulating sites

containing stable secondary structures, such as hairpins. To investigate this, we cloned luciferase reporter plasmids carrying target sites in which an 8mer or 7mer-A1 seed-binding site and a fully complementary (all-WC) 3'-pairing site were separated by a fourteen-nucleotide hairpin with a C(UUCG)G tetraloop (Figure 3E), which is a highly stable loop motif (50).

We found that these hairpin-containing sites were strongly downregulated by *miR-34a* in the presence of all-WC 3'-pairing (Figure 3F), with the 7mer-A1 site being somewhat more efficient than the equivalent site with a fourteen-nucleotide unstructured bulge (cf. Figure 3D, +14 all WC site). However, disruption of supplementary (t13–t16) pairing (ΔS) led to severe decreases in downregulation, with both the 8mer and 7mer-A1 targets mediating considerably less repression than their respective seed-only sites (Figure 3F). These results indicate that mRNA hairpins can be accommodated inside the target:RISC complex without a strong adverse impact on site efficiency, raising the possibility that sequences complementary to a miRNA 3'-pairing region that are far upstream of the nearest seed-binding site may be brought within the range of functional interaction by the formation of bridging structures. The ability of miRNAs to bind hairpin-containing sites has previously been established by an interaction between *miR-122* and hepatitis C viral RNA (51–53) where the binding appears to protect the viral RNA from 5' exonuclease activity. Here, we show that the presence of a hairpin within a miRNA target site does not in principle prevent strong downregulation. Indeed, for the 8mer site with full 3'-pairing, there is no difference between a four-nucleotide bulge and a fourteen-nucleotide hairpin (cf. Figure 2C, upper right, and Figure 3F).

Target site accessibility modulates repression dependent on 3'-pairing strength

Our investigation into the relative impact of different 3'-pairing regions of *miR-34a* showed that removing the possibility of pairing to the supplementary (g13–g16) and in some cases tail (g17–g22) region typically resulted in downregulation comparable to that mediated by seed binding alone (Figure 2C, ΔS and ΔT mutants). Notably, some targets with disrupted pairing to these regions were less efficient than their respective seed-only targets (Figure 2C, lower panels), suggesting that even in the artificial context of a reporter construct, differences in repression cannot be attributed to base-pairing alone. As the sequence differences between these sites are considerable, with mutations altering four (ΔC , ΔS) or six (ΔT) nucleotides in the 3'-pairing site, we hypothesized that the discrepancies could be attributed to changes in the structural accessibility of the site within the luciferase mRNA constructs.

To better understand the patterns of downregulation of targets in which we disrupted pairing to different 3'-pairing regions in *miR-34a* (Figure 2A), we performed thermodynamic RNA secondary structure predictions using the ViennaRNA package (44). All target sites in Figure 2A were included in the simulations, as well as the 8mer and 7mer-A1 seed-only sites (Figure 1E, F). We considered two binding models: (i) a one-step hybridization between the single-stranded target RNA and miRNA (single-stranded model), and (ii) a two-step process in which the Renilla luciferase mRNA must first unfold to expose the target site, which adds an energetic penalty depending on the target sequence (unfolding model). We considered pairing to the full *miR-34a* sequence (Figure 4A, B, upper panels) as well as pairing to the seed only (g1–g8) (Fig-

ure 4A, B, lower panels), to test the relevance of 3'-pairing. In both the single-stranded and unfolding models, we found a weak correlation between the predicted binding energy of the entire target:miRNA complex and the downregulation in the luciferase reporter assay ($R^2 = 0.29$ and $R^2 = 0.34$ respectively) (Figure 4A, B, upper panels, solid lines).

We next explored the possibility that the binding energy might be a better predictor of downregulation for some groups of mutants than for others. To this end, we separately analyzed correlation for sites with strong potential 3'-pairing (no mutation and ΔC) and sites with weaker potential 3'-pairing (ΔS , ΔT and seed-only). We found that the correlation between predicted binding energy and downregulation was higher for the former group (no mutation and ΔC ; Figure 4A, B, blue and purple dots, dashed lines) than for the latter (ΔS , ΔT and seed-only; Figure 4A, B, red, orange and black dots, dotted lines) when we considered pairing to the entire *miR-34a* sequence, whereas the opposite was true for the seed-only predictions (Figure 4A, B, cf. upper and lower panels). Notably, when we considered binding to the seed alone in the two-step model (Figure 4B, lower panel), the correlation between predicted binding energy and luciferase downregulation was strong for sites with weak 3'-pairing ($R^2 = 0.81$), but minimal for sites with strong 3'-pairing ($R^2 = 0.078$). In particular, in the unfolding model the two ΔS mutants which mediated the least repression had lower predicted seed interaction energy (calculated as the sum of the mRNA unfolding and miRNA binding energies) than the 8mer and 7mer-A1 seed-only targets.

Thus, the repression of sites with strong 3'-pairing correlated best with a model taking into account the mRNA unfolding energy and binding to the full miRNA, while repression of sites with weak 3'-pairing correlated best with a model taking into account unfolding and binding of the seed-binding site alone. This suggests that sites with weak 3'-pairing are particularly sensitive to the structural accessibility of the seed-binding site in the mRNA, while sites with strong 3'-pairing are efficiently repressed regardless of seed accessibility. We recognize that the predicted energies in the unfolding model vary with the choice of UTR termination site (Supplementary Figure S3A), which is likely to be variable in reality (54), but the conclusions are unaffected (Supplementary Figure S3B).

Based on these simulations, we propose a model in which one potential function of 3'-pairing is to stabilize a target:miRNA interaction in a way that can compensate for less-than-ideal initial binding conditions, such as a weak or structurally inaccessible seed-binding site (Figure 4C). Accordingly, if a site has limited potential for 3'-pairing the ability to establish an interaction with the seed in the first place becomes a stronger relative determinant of the final outcome.

3'-pairing can rescue sites with low seed accessibility

To experimentally test our proposed rescue model (Figure 4C), we designed two artificial *miR-34a* target sites, one with and one without potential 3'-pairing, in which the seed-binding site can pair to a complementary downstream sequence and form a stable hairpin (Figure 4D, structures 1 and 2). We probed these constructs with RABS to determine the combined impact of low seed accessibility and 3'-pairing on the interaction with *miR-34a*. In the unbound condition, both constructs with an inaccessible seed-binding site, with or without potential 3'-pairing, displayed low reactivities in the seed-



Figure 4. MiRNA 3'-pairing can rescue sites with low seed accessibility. **(A)** Correlation between target:*miR-34a* interaction energy in a one-step binding model (predicted with RNAcofold) and downregulation in luciferase reporter assays (Luciferase data were taken from Figure 2C and Figure 1F (seed-only sites), and is shown as the mean \pm standard deviation). **(B)** Correlation between target:*miR-34a* interaction energy in an unfolding/binding two-step model (predicted with RNAup) and downregulation in luciferase reporter assays. Constraints were imposed on the structure predictions as indicated in each plot. (Luciferase data same as above). **(C)** Proposed model for the capacity of strong 3'-pairing to compensate for suboptimal seed-binding conditions. **(D)** Predicted secondary structures of artificial *miR-34a* target sites with inaccessible seed and 3'-pairing sites as indicated. **(E)** Mean RABS reactivities ($n = 3$) of nucleotides in structures 1, 2 and 3 in (D), as indicated, in unbound form or bound to *miR-34a* or *miR-34a*:AGO2, where reactivities below 0.5 indicate base-pairing. **(F)** *MiR-34a* regulation of dual luciferase reporters after 24 h with the target sites in (D), with indicated mutations, transfected into HEK293T cells.

binding site and the complementary hairpin stem, but high reactivities everywhere else (Figure 4E). This suggests that the hairpin forms as predicted while the remaining nucleotides are accessible for pairing, with no additional interfering structure.

In the absence of available 3'-pairing, there were no changes in reactivity anywhere in the sequence upon addition of *miR-34a* or *miR-34a:AGO2* (Figure 4E, upper panel). Although we cannot directly distinguish between intra- and intermolecular pairing in this assay, we note that there was no increased reactivity in the hairpin stem, which would be expected if the seed-binding site was instead bound to the miRNA (thus releasing the hairpin stem to be modified by the 1M7 reagent). This indicates that the target hairpin structure predominates, preventing substantial interaction with the miRNA. By contrast, with full 3'-complementarity available upstream of the seed-binding site there was both substantial 3'-pairing and increased reactivity in the hairpin stem in the presence of *miR-34a* or *miR-34a:AGO2* (Figure 4E, middle panel), which suggests that under these conditions RISC is able to compete with the pre-existing target structure.

Although the reactivity also increased in the seed-binding site compared to the unbound form, it is important to consider that the measured reactivities reflect an equilibrium of multiple target:RISC interactions, and the overall reactivity changes in the stems suggest that the strong hairpin in the unbound condition has been destabilized. Considering the comparatively small differences in reactivity observed in the 3'-pairing site of the seed-scrambled control (Figure 1D, upper panel), it is unlikely that RISC would interact so strongly with the 3'-pairing site without any seed interaction.

Next, we wanted to investigate the case of an accessible seed-binding site and inaccessible potential 3'-pairing. To this end, we designed another construct in which the 3'-pairing site can bind to a complementary upstream sequence and form a hairpin, while the seed-binding site is unpaired (Figure 4D, structure 3). The RABS reactivity profile for this site in the absence of ligands was consistent with the predicted structure, with low reactivity in the hairpin stem regions compared to the loop and seed nucleotides (Figure 4E, lower panel). When RISC was added, we observed lower reactivities in the seed-binding site, indicating pairing to the miRNA. Reactivity changes in the 3'-pairing site were much smaller, indicating that the pre-existing structure prevents intermolecular pairing, although a small increase in reactivity in the hairpin stem relative to the 3'-pairing site suggests competition with pairing to the miRNA.

In order to test the impact of seed accessibility versus 3'-pairing on target repression, we generated luciferase plasmids carrying the sequences described above. For comparison, we also included matching target sites where the blocking stem sequence was removed, rendering the seed accessible for interaction (Figure 4D, structures 4 and 5). The site with an inaccessible seed and no potential 3'-pairing (structure 1) was not downregulated at all compared to a seed-scrambled control, consistent with the apparent lack of target:RISC interaction in the RABS experiment (Figure 4F, statistical analysis in Supplementary Figure S2C). An inaccessible seed with 3'-pairing (structure 2) resulted in comparable downregulation to an accessible seed with inaccessible 3'-pairing (structure 3) and an accessible seed without 3'-pairing (structure 4), with no statistically significant differences between any of the three sites. As expected, an accessible seed with 3'-pairing (structure 5) was most strongly repressed. These results suggest that pair-

ing beyond the seed can compensate for low seed accessibility, although not to the point of fully cancelling out the deleterious influence of a stable secondary mRNA structure.

Transcriptome-wide analysis demonstrates that sites with efficient 3'-pairing are less sensitive to low seed accessibility

After confirming the capacity of 3'-pairing to overcome an inaccessible seed-binding site and confer repression in a designed experimental system, we sought to examine how seed-binding site unfolding and miRNA binding energies predict downregulation across the transcriptome for sites with and without 3'-pairing (Figure 5A). We downloaded microarray datasets measuring responses to transfection of six miRNAs (Figure 5B) in HCT116 cells at 24 h (15,46). For each gene:miRNA combination, we examined target site predictions from the TargetScan database (15), focusing our analyses on genes with one 8mer or 7mer seed-binding site for the relevant miRNA. We checked each site for the presence of potential 3'-pairing (defined as at least four continuous Watson-Crick base-pairs to the g12-g17 region, with a maximum offset of four nucleotides on either the miRNA or the target side). For each target, we also predicted the unfolding energy of eight nucleotides spanning the seed-binding site ($\Delta G_{\text{unfolding}}$) with RNAup. The unfolding energy was summed with the predicted seed-binding energy ($\Delta G_{\text{binding}}$, calculated for each seed type of the miRNAs using the RNAeval module) to obtain the interaction energy for the seed.

When target sites were divided into bins by quartile of seed interaction energy ($\Delta G_{\text{unfolding}} + \Delta G_{\text{binding}}$), we found a steady decrease in mean downregulation (shown as a \log_2 fold change) with weaker predicted interaction (Figure 5C), as a proxy for the accessibility of the seed-binding site. Intriguingly, only two of the six miRNAs showed a statistically significant increase in downregulation with the presence of 3'-pairing (Figure 5D), indicating that the importance of pairing to the supplementary region may vary between miRNAs (see also (55)).

When all six miRNAs were grouped, sites with and without 3'-pairing were similarly affected by the seed interaction energy (Figure 5E, left panel, orange and blue bars). The same was true for the four miRNAs for which predicted 3'-pairing had no significant impact (Figure 5E, middle panel). However, for the remaining two miRNAs which displayed improved downregulation with functional 3'-pairing (Figure 5D), we saw diverging trends for sites with and without potential 3'-pairing (Figure 5E, right panel). The mean repression of sites without 3'-pairing showed a steady downward trend with decreasing seed accessibility, whereas for sites with 3'-pairing we observed a break in the trend, with an increase in mean repression in the quartile of lowest seed-binding site accessibility (weakest seed interaction). Although the small number of sites with 3'-pairing adds uncertainty to the analysis, these findings are consistent with strong 3'-pairing decreasing the sensitivity of target site repression to seed-binding site accessibility.

3'-pairing rescues an inaccessible seed in a naturally occurring target site

After validating the model using artificial target sites, we looked for human biological target sites with relevant structural properties (Figure 5F). To this end, we downloaded predicted binding sites from the TargetScan database (15)

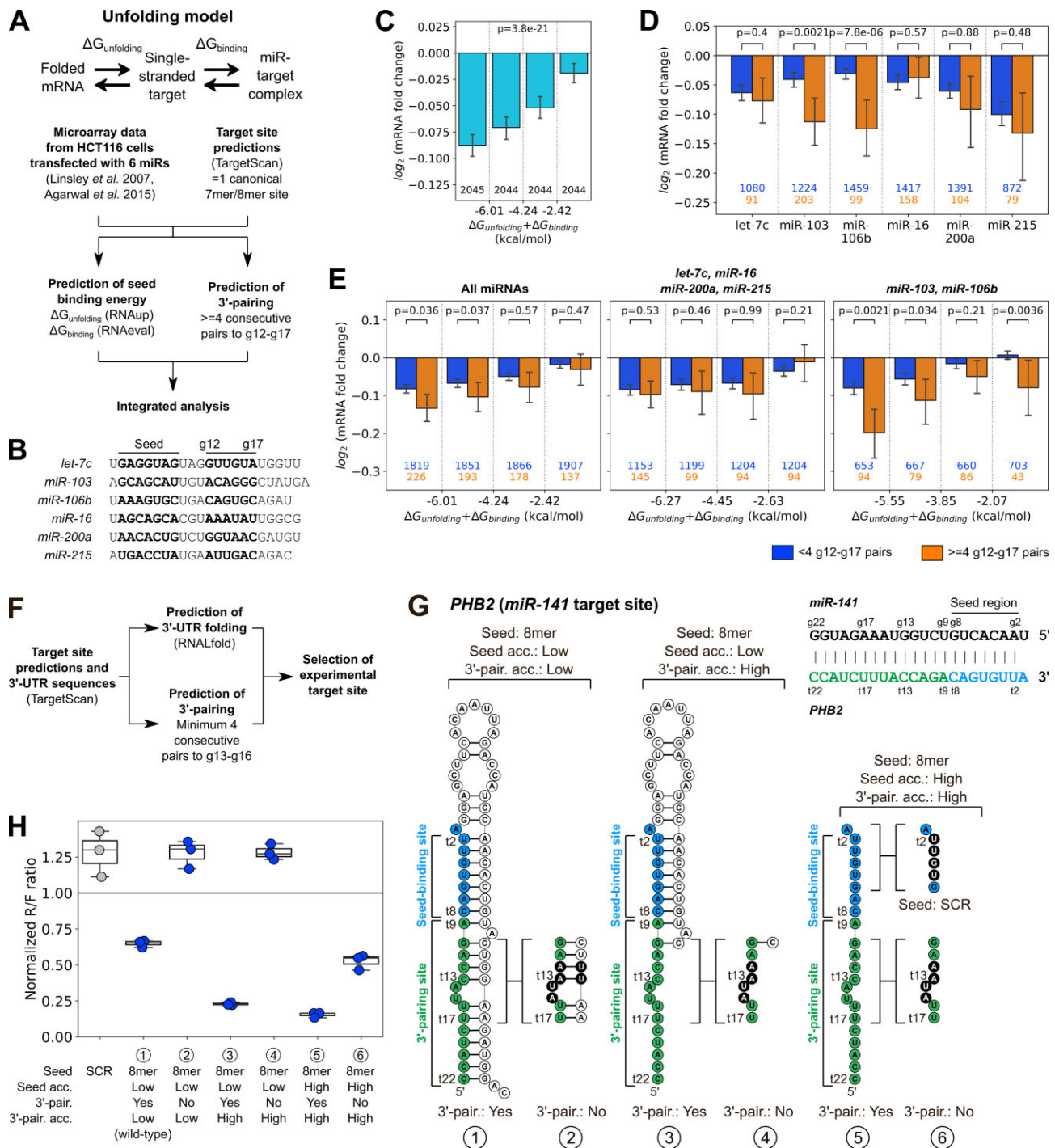


Figure 5. Validation of the 3'-pairing rescue model in biological target sites. **(A)** Pipeline for the analysis of interplay between seed accessibility and 3'-pairing at the transcriptomic level. **(B)** Sequences of miRNAs in the dataset. **(C)** Mean \log_2 fold change in each quartile of seed interaction strength ($\Delta G_{\text{unfolding}} + \Delta G_{\text{binding}}$) for all miRNAs. **(D)** Effect of predicted 3'-pairing on downregulation for each miRNA. Plots show the mean \log_2 fold change with 95% confidence intervals. **(E)** Mean \log_2 fold change in each quartile of seed interaction strength ($\Delta G_{\text{unfolding}} + \Delta G_{\text{binding}}$) for sites with (orange bars) and without (blue bars) predicted 3'-pairing, for indicated groups of miRNAs. Error bars in (C–E) indicate 95% confidence intervals. Statistical significance was tested by a one-way ANOVA (C) or Wilcoxon's ranksums test (D–E). **(F)** Pipeline for the discovery of targets with inaccessible seed-binding sites for experimental validation. **(G)** Predicted secondary structures of wild-type and mutant variants of the *miR-141* target site in *PHB2*. **(H)** *miR-141* regulation of dual luciferase reporters after 24 h with the target sites in **(G)**, with indicated mutations, transfected into HEK293T cells. Each datapoint represents an independent experiment ($n = 3$).

for miRNAs from broadly conserved seed families. For target:miRNA complexes with substantial 3'-pairing (at minimum, full canonical WC pairing to g13–g16, with at most a four-nucleotide bulge on the target side), we predicted an ensemble of locally stable secondary structures in the 3'-UTR using RNAfold (44). We searched for target site folds with a predicted minimum free energy (MFE) lower than -10 kcal/mol, in which at least five bases in the seed-binding site were paired downstream, and where this fold was present in at least 75% of all structures spanning the target site. We found 1136 (2.6%) target:miRNA pairs with a predicted UTR fold meeting these criteria out of 43 922 pairs with 3'-pairing, although these numbers vary greatly depending on the precise definition of 3'-pairing and selection criteria for target site folds chosen.

From these candidates, we selected the interaction between *miR-141* and its binding site in *prohibitin 2* (*PHB2*). This site, which consists of an 8mer seed-binding site and full 3'-pairing complementarity, has the potential to be completely blocked by a hairpin structure in its native transcript (Figure 5G, structure 1). This structure is highly stable, with a predicted MFE of -28.0 kcal/mol, and no competing 3'-UTR folds spanning the *miR-141* target site were present in the ensemble. Importantly, the fold maintained its predicted structure in response to mutations in the target sequence.

To test the potential influence of this structure on *miR-141*-mediated downregulation, we cloned luciferase plasmids carrying the full-length hairpin (Figure 5G, structure 1), as well as variants in which only the seed-binding site was inaccessible (Figure 5G, structure 3) or the entire target site was accessible (Figure 5G, structure 5). For each variant, we also mutated part of the 3'-pairing site (t12–t15) to disrupt the interaction with *miR-141* (Figure 5G, structures 2, 4 and 6). When necessary, corresponding mutations were introduced in the hairpin stem to preserve the overall structure. We found that the wild-type target site within the full hairpin was moderately downregulated by *miR-141* (Figure 5H, structure 1, statistical analysis in Supplementary Figure S2D). However, when 3'-pairing was disrupted (structure 2), the level of repression was similar to the seed-scrambled control. Making the 3'-pairing site accessible by removing part of the hairpin substantially increased downregulation (structure 3), but again disrupting pairing beyond the seed (structure 4) led to a complete loss of functionality, indicating that in both cases where the miRNA has to compete with a prior mRNA structure to initiate seed binding, the additional pairing is required for observable repression. When the seed-binding site was accessible (structure 5), mutating the t12–t15 residues decreased downregulation (structure 6) but the site remained viable, comparable to the *SIRT1* Δ S (t13–t16) mutants (cf. Figure 2C, lower right panel).

Discussion

The functional role of pairing beyond the seed in miRNA target selection referred to as 3'-pairing, remains an important question. Here, we used the *SIRT1:miR-34a* complex, which has previously been studied by NMR (8), as a model system for studying the interaction between seed pairing, 3'-pairing and target site accessibility in determining the degree of repression mediated by a miRNA target site. Using RABS (33) for determination of secondary structure *in vitro* and luciferase reporter assays to measure downregulation in cells, we found

that for sites with weak 3'-pairing, repression correlates well with the combined predicted Δ G of seed unfolding and subsequent binding to the miRNA (Figure 4B, lower panel, dotted line), whereas sites with stronger 3'-pairing were less sensitive to seed-site accessibility. We further demonstrate that hairpin structures blocking a miRNA binding site can reduce target:miRNA interactions to non-functional levels when only seed pairing is available, but that 3'-pairing can overcome this hindrance and enable significant downregulation. Analysis of transcriptomic-wide response to miRNA overexpression supported a degree of differential sensitivity to seed accessibility for target sites with and without effective 3'-pairing. Our results thus suggest that 3'-pairing can play an important role in compensating for suboptimal initial seed-binding conditions.

The supplementary and tail regions of miR-34a both enhance target repression

With regards to the different sub-regions of 3'-pairing, our findings are broadly compatible with prior data emphasizing the supplementary region (comprising, at minimum, residues g13 to g16), while also showing substantial contribution from the tail region (g17–g22). Conversely, pairing to the central g9–g12 region had low impact on repression, consistent with a recently published crystal structure of a target:RISC complex in which the miRNA binds to the seed and supplementary regions of the target but not to the central residues, even though they are complementary (24). We note that *miR-34a* has G residues at positions 17–18, which means that if full 3'-end pairing is available, this region would be expected to make a significant energetic contribution towards stabilizing the target:miRNA helix. This would be in line with recent studies showing that the binding preferences of different miRNAs vary depending on their 3'-end sequence (10,56). Importantly, our data suggests that even in a reporter assay context, target:miRNA base-pairing differences alone are not sufficient to explain variations in outcome.

Choice of Ago paralog for RABS experiments

This work aimed to determine the function of 3'-pairing in mediating repression, with an emphasis not only on sequence and binding strength, but also on structure. We therefore predicted the structure adopted by target:miRNA complexes using ViennaRNA modules, and validated these using RABS to confirm that repression efficiency, assessed in luciferase assays, reflected our predicted pairing and structure. RABS was performed with *miR-34a*, or *miR-34a* loaded into AGO2. In human cells, other Ago paralogs are present that could influence target repression (57). Ago paralogs largely load similar populations of miRNAs, but do exhibit some differential miR loading (58) as well as paralog-specific repressive functions (57). AGO2 has long been thought of as the only paralog with slicing activity (59,60) but AGO3 can also mediate slicing, in a guide RNA-specific manner (61). Therefore, the dual luciferase reporter results do not purely reflect the target recognition by AGO2 in the cell. However, inducible knock-downs of individual Ago proteins in HEK293T cells indicate that AGO2 has a larger effect on miRNA-mediated regulation in this cell line than the other paralogs (62). Thus, we believe that the structures inferred from RABS experiments with *miR-34a*:AGO2 can be meaningfully related to the observed repression of the reporter proteins.

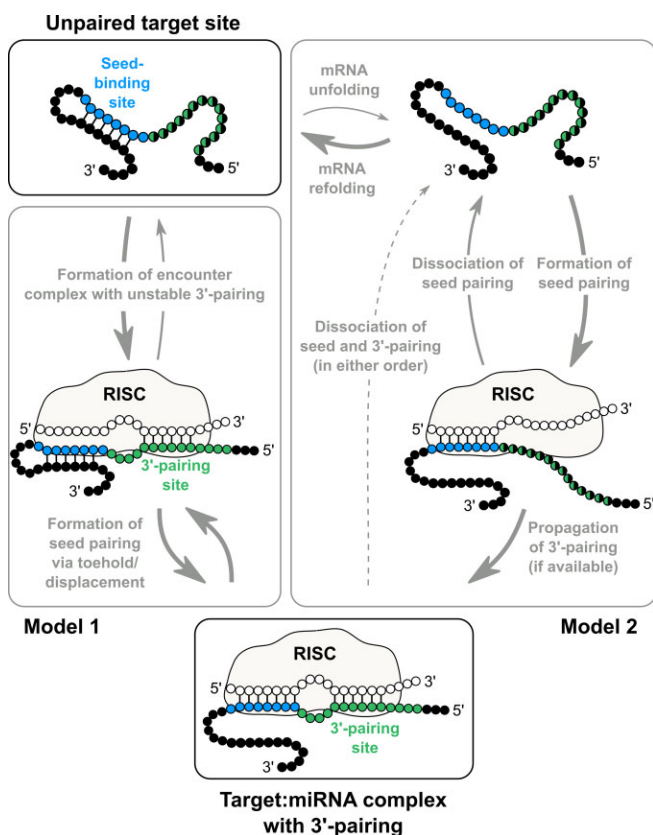


Figure 6. Possible mechanisms of 3'-pairing rescue. In Model 1, the 3'-pairing site assists the formation of a transient encounter complex, which is then stabilized by seed pairing displacing the mRNA self-pairing via a toehold mechanism. In Model 2, the mRNA unfolds independently of the miRNA, but the unfavourability of this reaction is compensated for by slower dissociation of the miRNA from its target due to increased stability from 3'-pairing, relative to a target with seed-only pairing.

Mechanistic implications for miRNA binding

Based on structural and functional data from RABS and reporter assays, we propose a model in which the negative effect on site efficiency of secondary structures in an mRNA restricting the formation of target:miRNA interactions can be partially offset by 3'-pairing, enabling downregulation of the gene product (Figure 4C). This potential compensatory role of 3'-pairing could be seen as a parallel to the so-called 3'-compensatory target sites (19,25), in which mismatches or single-nucleotide bulges inside the seed helix are tolerated due to pairing beyond the seed. Although our data do not provide insight into the step-by-step kinetics of the binding process, at least two models could plausibly explain our observations (Figure 6).

One possibility is that RISC directly causes unwinding of the helix blocking the seed-binding site. In this scenario, an extensive 3'-pairing site may transiently interact with the miRNA, forming an unstable encounter complex. This could allow time for seed pairing to form via the replacement of mRNA self-pairing by mRNA:miRNA pairing (Figure 6, 'Model 1'). Speculatively, this could involve a strand displacement mechanism, where an invading RNA strand (here the miRNA guide) pairs to a single-stranded region (called a toehold) that was previously paired to an incumbent strand (here another part of the mRNA), potentially leading to full displacement of the incumbent strand by the invading strand

(63). This mechanism allows for competitive binding even if the energetic barrier to spontaneous dissociation of the incumbent strand is high, as fraying of single base-pairs can be sufficient to form the toehold. Note that such a mechanism does not require RISC to possess any helicase activity.

Another possibility is that the mRNA must independently unfold to expose the seed-binding site prior to miRNA binding, but that the presence of substantial 3'-pairing limits subsequent miRNA dissociation and thus compensates for the decreased number of initial target:miRNA interactions when the seed is less accessible (Figure 6, 'Model 2'). In a physiological context, the structure of a 3'-UTR is likely variable due to ribosome movement (28), interactions with RNA-binding proteins (29) and competition with alternative internal structures. Consequently, even a strong blocking structure is unlikely to fully prevent the formation of target:miRNA interactions, but in some cases seed pairing alone may be insufficient to overcome the energetic penalty imposed by the necessity for preliminary target site unfolding, requiring increased target:miRNA affinity through more extensive base-pairing. Notably, we observed moderate repression of the wild-type *PHB2:miR-141* complex (Figure 5G, H), in which both the seed- and 3'-pairing sites are fully bound to downstream residues. In this case, some degree of spontaneous mRNA unfolding is required for any interaction with the miRNA to occur, assuming the sequence folds as predicted *in vivo*.

In a situation where the seed is freely accessible to bind but potential 3'-pairing is blocked, our results indicate that the 3'-pairing does not contribute to increased repression relative to the seed by itself (Figure 4F). This is either because the formation of a target:miRNA seed interaction does not by itself lead to the unfolding of adjacent secondary structures, or alternatively because the hairpin interferes with the diffusion of RISC along the mRNA (48,49) and thus limits the initial seed-binding step. However, as RISC moves along the mRNA from the 3' end, a structured element immediately upstream of the seed would be expected to interfere less than a downstream one. Indeed, the repression of sites with an internal hairpin shows that structures in the vicinity of the seed are not necessarily strongly detrimental to the formation of a target:miRNA complex (Figure 3E, F).

Concluding remarks

In summary, our data demonstrates that one potential function of miRNA pairing beyond the seed is to compensate for a structurally inaccessible seed-binding site, with strong 3'-pairing having the capacity to overcome a maximally inaccessible seed-binding site and substantially downregulate a target site that would otherwise be non-functional. Our results further suggest that it may sometimes be useful to consider the structural accessibility of different regions of a miRNA target site separately, as a seed-bound miRNA may not be able to compete for 3'-pairing with mRNA structures further upstream. We propose that such considerations can be useful for prediction of effective miRNA target sites as well as design of siRNAs.

Data availability

Raw data from structural probing, luciferase reporter assays, secondary structure predictions and analysis code are included as supplementary files.

Supplementary data

Supplementary Data are available at NAR Online.

Acknowledgements

T7 polymerase and iPPase used for *in vitro* transcription were produced at the Protein Science Facility (PSF) at Karolinska Institutet. Fragment length analysis of all RABS samples were performed at KIGene Core Facility. We thank members of the Petzold and Andersson labs for discussion.

Author contributions: D.M.K., E.B., K.P. and E.R.A. designed experiments and analyzed the data. D.M.K. performed the plasmid cloning, reporter assays and bioinformatic analyses. E.B. performed the RABS experiments. W.B. produced the AGO2 protein for the RABS experiments. D.M.K., K.P. and E.R.A. wrote the paper with input from all authors.

Funding

Knut and Alice Wallenberg Foundation collaborative project grant [KAW 2016.0087 to K.P. and E.R.A.]; K.P. further acknowledges support from Karolinska Institutet (KI Career Ladder positions) and Cancerfonden [21 1770 Pj]; E.R.A. further acknowledges support from Karolinska Institutet (KI Career Ladder positions). Funding for open access charge: Knut and Alice Wallenberg Foundation [KAW 2016.0087].

Conflict of interest statement

None declared.

References

- Friedman, R.C., Farh, K.K.H., Burge, C.B. and Bartel, D.P. (2009) Most mammalian mRNAs are conserved targets of microRNAs. *Genome Res.*, **19**, 92–105.
- Grimson, A., Farh, K.K.H., Johnston, W.K., Garrett-Engle, P., Lim, L.P. and Bartel, D.P. (2007) MicroRNA targeting specificity in mammals: determinants beyond seed pairing. *Mol. Cell*, **27**, 91–105.
- Wee, L.M., Flores-Jasso, C.F., Salomon, W.E. and Zamore, P.D. (2012) Argonaute divides its RNA guide into domains with distinct functions and RNA-binding properties. *Cell*, **151**, 1055–1067.
- Moore, M.J., Scheel, T.K.H., Luna, J.M., Park, C.Y., Fak, J.J., Nishiuchi, E., Rice, C.M. and Darnell, R.B. (2015) MiRNA-target chimeras reveal miRNA 3'-end pairing as a major determinant of Argonaute target specificity. *Nat. Commun.*, **6**, 8864.
- Weill, N., Lisi, V., Scott, N., Dallaire, P., Pelloux, J. and Major, F. (2015) MiRBooking simulates the stoichiometric mode of action of microRNAs. *Nucleic Acids Res.*, **43**, 6730–6738.
- Broughton, J.P., Lovci, M.T., Huang, J.L., Yeo, G.W. and Pasquinelli, A.E. (2016) Pairing beyond the seed supports microRNA targeting specificity. *Mol. Cell*, **64**, 320–333.
- McGeary, S.E., Lin, K.S., Shi, C.Y., Pham, T.M., Bisaria, N., Kelley, G.M. and Bartel, D.P. (2019) The biochemical basis of microRNA targeting efficacy. *Science*, **366**, eaav1741.
- Baronti, L., Guzzetti, I., Ebrahimi, P., Friebe Sandoz, S., Steiner, E., Schlagnitweit, J., Fromm, B., Silva, L., Fontana, C., Chen, A.A., *et al.* (2020) Base-pair conformational switch modulates miR-34a targeting of Sirt1 mRNA. *Nature*, **583**, 139–144.
- Kilikevicius, A., Meister, G. and Corey, D.R. (2022) Reexamining assumptions about miRNA-guided gene silencing. *Nucleic Acids Res.*, **50**, 617–634.
- McGeary, S.E., Bisaria, N., Pham, T.M., Wang, P.Y. and Bartel, D.P. (2022) MicroRNA 3'-compensatory pairing occurs through two binding modes, with affinity shaped by nucleotide identity and position. *eLife*, **11**, e69803.
- Soutschek, M., Gross, F., Schratt, G. and Germain, P.-L. (2022) scanMiR: a biochemically based toolkit for versatile and efficient microRNA target prediction. *Bioinformatics*, **38**, 2466–2473.
- Bartel, D.P. (2018) Metazoan microRNAs. *Cell*, **173**, 20–51.
- Lai, E.C. (2002) Micro RNAs are complementary to 3' UTR sequence motifs that mediate negative post-transcriptional regulation. *Nat. Genet.*, **30**, 363–364.
- Lewis, B.P., Shih, I.H., Jones-Rhoades, M.W., Bartel, D.P. and Burge, C.B. (2003) Prediction of mammalian microRNA targets. *Cell*, **115**, 787–798.
- Agarwal, V., Bell, G.W., Nam, J.W. and Bartel, D.P. (2015) Predicting effective microRNA target sites in mammalian mRNAs. *eLife*, **4**, e05005.
- Abbott, A.L., Alvarez-Saavedra, E., Miska, E.A., Lau, N.C., Bartel, D.P., Horvitz, H.R. and Ambros, V. (2005) The let-7 microRNA family members mir-48, mir-84, and mir-241 function together to regulate developmental timing in *Caenorhabditis elegans*. *Dev. Cell*, **9**, 403–414.
- Alvarez-Saavedra, E. and Horvitz, H.R. (2010) Many families of *C. elegans* microRNAs are not essential for development or viability. *Curr. Biol.*, **20**, 367–373.
- Doench, J.G. and Sharp, P.A. (2004) Specificity of microRNA target selection in translational repression. *Genes Dev.*, **18**, 504–511.
- Brennecke, J., Stark, A., Russell, R.B. and Cohen, S.M. (2005) Principles of microRNA-target recognition. *PLoS Biol.*, **3**, 0404–0418.
- Lai, E.C., Tam, B. and Rubin, G.M. (2005) Pervasive regulation of *Drosophila* Notch target genes by GY-box-, brd-box-, and K-box-class microRNAs. *Genes Dev.*, **19**, 1067–1080.
- Lim, L.P., Lau, N.C., Garrett-Engle, P., Grimson, A., Schelter, J.M., Castle, J., Bartel, D.P., Linsley, P.S. and Johnson, J.M. (2005) Microarray analysis shows that some microRNAs downregulate large numbers of target mRNAs. *Nature*, **433**, 769–773.
- Wahlquist, C., Jeong, D., Rojas-Muñoz, A., Kho, C., Lee, A., Mitsuyama, S., Van Mil, A., Jin Park, W., Sluijter, J.P.G., Doevendans, P.A.F., *et al.* (2014) Inhibition of miR-25 improves cardiac contractility in the failing heart. *Nature*, **508**, 531–535.
- Schirle, N.T., Sheu-Gruttadauria, J. and MacRae, I.J. (2014) Structural basis for microRNA targeting. *Science*, **346**, 608–613.
- Sheu-Gruttadauria, J., Xiao, Y., Gebert, L.F. and MacRae, I.J. (2019) Beyond the seed: structural basis for supplementary microRNA targeting by human Argonaute2. *EMBO J.*, **38**, e101153.
- Vella, M.C., Choi, E.Y., Lin, S.Y., Reinert, K. and Slack, F.J. (2004) The *C. elegans* microRNA let-7 binds to imperfect let-7 complementary sites from the lin-41 3'UTR. *Genes Dev.*, **18**, 132–137.
- Brown, K.M., Chu, C. and Rana, T.M. (2005) Target accessibility dictates the potency of human RISC. *Nat. Struct. Mol. Biol.*, **12**, 469–470.
- Kertesz, M., Iovino, N., Unnerstall, U., Gaul, U. and Segal, E. (2007) The role of site accessibility in microRNA target recognition. *Nat. Genet.*, **39**, 1278–1284.
- Ruijtenberg, S., Sonneveld, S., Cui, T.J., Logister, I., de Steenwinkel, D., Xiao, Y., MacRae, I.J., Joo, C. and Tanenbaum, M.E. (2020) mRNA structural dynamics shape argonaute-target interactions. *Nat. Struct. Mol. Biol.*, **27**, 790–801.
- Kim, S., Kim, S., Chang, H.R., Kim, D., Park, J., Son, N., Park, J., Yoon, M., Chae, G., Kim, Y.-K., *et al.* (2021) The regulatory impact of RNA-binding proteins on microRNA targeting. *Nat. Commun.*, **12**, 5057.
- Rokavec, M., Li, H., Jiang, L. and Hermeking, H. (2014) The p53/miR-34 axis in development and disease. *J. Mol. Cell Biol.*, **6**, 214–230.

31. Yamakuchi, M., Ferlito, M. and Lowenstein, C.J. (2008) miR-34a repression of SIRT1 regulates apoptosis. *Proc. Natl. Acad. Sci. U.S.A.*, **105**, 13421–13426.
32. Willkomm, S., Jakob, L., Kramm, K., Graus, V., Neumeier, J., Meister, G. and Grohmann, D. (2022) Single-molecule FRET uncovers hidden conformations and dynamics of human Argonaute 2. *Nat. Commun.*, **13**, 3825.
33. Banijamali, E., Baronti, L., Becker, W., Sajkowska-Kozielewicz, J.J., Huang, T., Palka, C., Kosek, D., Sweetapple, L., Müller, J., Stone, M.D., *et al.* (2023) RNA:RNA interaction in ternary complexes resolved by chemical probing. *RNA*, **29**, 317–329.
34. Salzman, D.W., Nakamura, K., Nallur, S., Dookwah, M.T., Metheerairut, C., Slack, F.J. and Weidhaas, J.B. (2016) miR-34 activity is modulated through 5'-end phosphorylation in response to DNA damage. *Nat. Commun.*, **7**, 10954.
35. Pall, G.S. and Hamilton, A.J. (2008) Improved northern blot method for enhanced detection of small RNA. *Nat. Protoc.*, **3**, 1077–1084.
36. Tian, S. and Das, R. (2017) Primerize-2D: automated primer design for RNA multidimensional chemical mapping. *Bioinformatics*, **33**, 1405–1406.
37. Borkotoky, S. and Murali, A. (2018) The highly efficient T7 RNA polymerase: a wonder macromolecule in biological realm. *Int. J. Biol. Macromol.*, **118**, 49–56.
38. Kern, J.A. and Davis, R.H. (1997) Application of solution equilibrium analysis to in vitro RNA transcription. *Biotechnol. Prog.*, **13**, 747–756.
39. Cordero, P., Kladwang, W., VanLang, C.C. and Das, R. (2014) The mutate-and-map protocol for inferring base pairs in structured RNA. In: *RNA Folding. Methods in Molecular Biology (Methods and Protocols)*. pp. 53–77.
40. Mortimer, S.A. and Weeks, K.M. (2007) A fast-acting reagent for accurate analysis of RNA secondary and tertiary structure by SHAPE chemistry. *J. Am. Chem. Soc.*, **129**, 4144–4145.
41. Lee, S., Kim, H., Tian, S., Lee, T., Yoon, S. and Das, R. (2015) Automated band annotation for RNA structure probing experiments with numerous capillary electrophoresis profiles. *Bioinformatics*, **31**, 2808–2815.
42. Washietl, S., Hofacker, I.L., Stadler, P.F. and Kellis, M. (2012) RNA folding with soft constraints: reconciliation of probing data and thermodynamic secondary structure prediction. *Nucleic Acids Res.*, **40**, 4261–4272.
43. Wilkinson, K.A., Gorelick, R.J., Vasa, S.M., Guex, N., Rein, A., Mathews, D.H., Giddings, M.C. and Weeks, K.M. (2008) High-throughput SHAPE analysis reveals structures in HIV-1 genomic RNA strongly conserved across distinct biological states. *PLoS Biol.*, **6**, e96.
44. Lorenz, R., Bernhart, S.H., Höner zu Siederdissen, C., Tafer, H., Flamm, C., Stadler, P.F. and Hofacker, I.L. (2011) ViennaRNA package 2.0. *Algorithms Mol. Biol.*, **6**, 26.
45. Reuter, J.S. and Mathews, D.H. (2010) RNAstructure: software for RNA secondary structure prediction and analysis. *BMC Bioinf.*, **11**, 129.
46. Linsley, P.S., Schelter, J., Burchard, J., Kikukawa, M., Martin, M.M., Bartz, S.R., Johnson, J.M., Cummins, J.M., Raymond, C.K., Dai, H., *et al.* (2007) Transcripts targeted by the microRNA-16 family cooperatively regulate cell cycle progression. *Mol. Cell. Biol.*, **27**, 2240–2252.
47. Tafer, H., Ameres, S.L., Obernosterer, G., Gebeshuber, C.A., Schroeder, R., Martinez, J. and Hofacker, I.L. (2008) The impact of target site accessibility on the design of effective siRNAs. *Nat. Biotechnol.*, **26**, 578–583.
48. Salomon, W.E., Jolly, S.M., Moore, M.J., Zamore, P.D. and Serebrov, V. (2015) Single-molecule imaging reveals that Argonaute reshapes the binding properties of its nucleic acid guides. *Cell*, **162**, 84–95.
49. Chandradoss, S.D., Schirle, N.T., Szczepaniak, M., MacRae, I.J. and Joo, C. (2015) A dynamic search process underlies microRNA targeting. *Cell*, **162**, 96–107.
50. Tuerk, C., Gauss, P., Thermes, C., Groebe, D.R., Gayle, M., Guild, N., Stormo, G., D'Aubenton-Carafa, Y., Uhlenbeck, O.C. and Tinoco, I. (1988) CUUCG hairpins: extraordinarily stable RNA secondary structures associated with various biochemical processes. *Proc. Natl. Acad. Sci.*, **85**, 1364–1368.
51. Machlin, E.S., Sarnow, P. and Sagan, S.M. (2011) Masking the 5' terminal nucleotides of the hepatitis C virus genome by an unconventional microRNA-target RNA complex. *Proc. Natl. Acad. Sci. U.S.A.*, **108**, 3193–3198.
52. Shimakami, T., Yamane, D., Jangra, R.K., Kempf, B.J., Spaniel, C., Barton, D.J. and Lemon, S.M. (2012) Stabilization of hepatitis C virus RNA by an Ago2-miR-122 complex. *Proc. Natl. Acad. Sci. U.S.A.*, **109**, 941–946.
53. Gebert, L.F.R., Law, M. and MacRae, I.J. (2021) A structured RNA motif locks Argonaute2:miR-122 onto the 5' end of the HCV genome. *Nat. Commun.*, **12**, 6836.
54. Neve, J., Patel, R., Wang, Z., Louey, A. and Furger, A.M. (2017) Cleavage and polyadenylation: ending the message expands gene regulation. *RNA Biol.*, **14**, 865–890.
55. Becker, W.R., Ober-Reynolds, B., Jouravleva, K., Jolly, S.M., Zamore, P.D. and Greenleaf, W.J. (2019) High-throughput analysis reveals rules for target RNA binding and cleavage by AGO2. *Mol. Cell*, **75**, 741–755.
56. Duan, Y., Veksler-Lublinsky, I. and Ambros, V. (2022) Critical contribution of 3' non-seed base pairing to the *in vivo* function of the evolutionarily conserved let-7a microRNA. *Cell Rep.*, **39**, 110745.
57. Nakanishi, K. (2022) Anatomy of four human Argonaute proteins. *Nucleic Acids Res.*, **50**, 6618–6638.
58. Azuma-Mukai, A., Oguri, H., Mituyama, T., Qian, Z.R., Asai, K., Siomi, H. and Siomi, M.C. (2008) Characterization of endogenous human argonautes and their miRNA partners in RNA silencing. *Proc. Natl. Acad. Sci. U.S.A.*, **105**, 7964–7969.
59. Meister, G., Landthaler, M., Patkaniowska, A., Dorsett, Y., Teng, G. and Tuschl, T. (2004) Human Argonaute2 mediates RNA cleavage targeted by miRNAs and siRNAs. *Mol. Cell*, **15**, 185–197.
60. Liu, J., Carmell, M.A., Rivas, F.V., Marsden, C.G., Thomson, J.M., Song, J.-J., Hammond, S.M., Joshua-Tor, L. and Hannon, G.J. (2004) Argonaute2 is the catalytic engine of mammalian RNAi. *Science*, **305**, 1437–1441.
61. Park, M.S., Phan, H.-D., Busch, F., Hinckley, S.H., Brackbill, J.A., Wysocki, V.H. and Nakanishi, K. (2017) Human Argonaute3 has slicer activity. *Nucleic Acids Res.*, **45**, 11867–11877.
62. Schmitter, D., Filkowski, J., Sewer, A., Pillai, R.S., Oakeley, E.J., Zavolan, M., Svoboda, P. and Filipowicz, W. (2006) Effects of Dicer and Argonaute down-regulation on mRNA levels in human HEK293 cells. *Nucleic Acids Res.*, **34**, 4801–4815.
63. Hong, F. and Sulc, P. (2019) An emergent understanding of strand displacement in RNA biology. *J. Struct. Biol.*, **207**, 241–249.